Precise Motion Compensation Approach for High-Resolution Multirotor UAV SAR in the Presence of Multiple Errors

Jiahao Han [ID], Shiyang Tang [ID], *Member, IEEE*, Zhanye Chen [ID], Yi Ren, Zhixin Lian [ID], Ping Guo [ID], Yinan Li, *Member, IEEE*, Linrang Zhang, and Hing Cheung So [ID], *Fellow, IEEE*

Abstract—As an important supplement to traditional airborne synthetic aperture radar (SAR), multirotor unmanned aerial vehicle (UAV) SAR has the advantages of low cost, high flexibility, and strong survival ability. However, due to the complex motion and flight characteristics of the multirotor UAV platform, multirotor UAV SAR faces challenges, including spatially variant low-frequency (LF) errors and severe high-frequency (HF) errors. To deal with these problems, an improved motion compensation approach is proposed for multirotor UAV SAR imaging, which is implemented through two processing steps. 1) The LF errors are eliminated by an improved two-step MoCo approach, which takes into account the spatial variations of both envelope and phase. 2) The HF errors are estimated and corrected by an extended phase gradient autofocus scheme. Different from conventional solutions, our approach can effectively remove the complex motion errors of multirotor UAV SAR step-by-step with high robustness even in high-resolution scenarios. Computer simulation and experimental results verify the effectiveness of our approach.

Index Terms—High-frequency (HF) error, low-frequency (LF) error, motion compensation (MOCO), multirotor unmanned aerial vehicle (UAV), synthetic aperture radar (SAR).

I. INTRODUCTION

SYNTHETIC aperture radar (SAR) utilizes pulse compression and coherent integration of a series of wideband signals

Jiahao Han, Shiyang Tang, Yi Ren, Zhixin Lian, and Linrang Zhang are with the National Key Laboratory of Radar Signal Processing, Xidian University, Xi'an 710071, China (e-mail: sytang@xidian.edu.cn).

Zhanye Chen is with the State Key Laboratory of Millimeter Waves, Southeast University, Nanjing 210096, China, and also with the Institute of Electromagnetic Space, Southeast University, Nanjing 210096, China (e-mail: xdczy@hotmail.com).

Ping Guo is with the College of Communication and Information Engineering, Xi'an University of Science and Technology, Xi'an 710054, China (e-mail: guopingxidian@126.com).

Yinan Li is with the National Key Laboratory of Radar Signal Processing, Xidian University, Xi'an 710071, China, and also with the China Academy of Space Technology, Xi'an 710100, China (e-mail: liyn@cast504.com).

Hing Cheung So is with the Department of Electrical Engineering, City University of Hong Kong, Hong Kong (e-mail: hcso@ee.cityu.edu.hk).

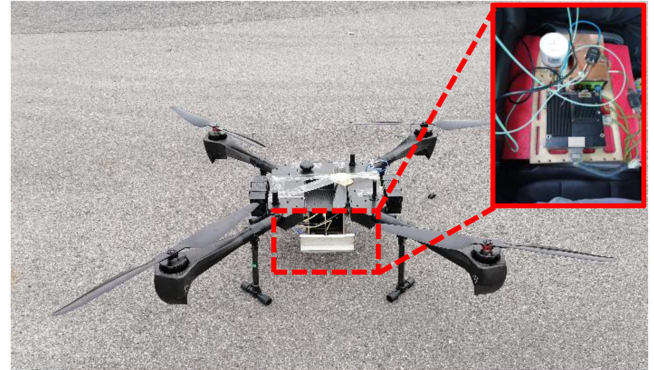Digital Object Identifier 10.1109/JSTARS.2024.3449318

Fig. 1. Multirotor UAV SAR system.

to obtain high-resolution 2-D images [1]. Over the past few decades, due to its high level of flexibility, airborne SAR has gained widespread attention across numerous fields, including target recognition, remote sensing mapping, and military reconnaissance [2], [3]. Recently, thanks to the trend of miniaturization and lightweightness in SAR systems, it can be integrated with diverse unmanned aerial vehicle (UAV) platforms, particularly small multirotor UAVs, to further leverage its strengths and broaden its applicability [4], [5], [6], [7]. As shown in Fig. 1, the SAR system is installed on the multirotor UAV platform, with weight and antenna size of approximately 4 kg and 15 cm × 24 cm, respectively. The system is powered by a 10 000 mA battery. As a beneficial supplement to the traditional airborne SAR, multirotor UAV SAR has the characteristics of low cost and simple operation, making it ideally suited for civilian contexts, such as environmental protection, resource exploration, agricultural production, and emergency rescue, and has therefore become another research hotspot in the SAR field [5], [6], [7], [8], [9], [10].

Despite its high potential, multirotor UAV SAR has not been popularized in practice mainly because of the following limitations. First, the multirotor UAV is easily affected by atmospheric turbulence due to its small size and lightweight, leading to significant low-frequency (LF) errors [11], [12]. In this case, both the phase and envelope spatial variations caused by LF errors cannot be ignored; otherwise, they will defocus the SAR images [13], [14], [15]. Second, the flight state of the multirotor

UAV is influenced by the rotation of the propellers, introducing high-frequency (HF) errors [16], [17]. Although the amplitude of these HF errors is generally very small, they can introduce paired false targets in SAR images, seriously degrading the imaging qualities [18], [19], [20]. Consequently, to fully exert the advantages of multirotor UAV SAR, it is necessary to propose a motion compensation (MoCo) approach applicable to multirotor UAV SAR with complex motion errors.

For LF errors, Bezvesilniy et al. [21] proposed a phase error estimation method based on local-quadratic map-drift (MD). This method can construct the complete LF error compensation function by integrating the estimated local quadratic phase errors without splicing. Wu et al. [22] presented an autofocus method based on the minimum entropy criterion to remove the nonlinear LF phase errors, which does not require separating strong targets in the image domain, implying broader applicability. However, the authors in [21] and [22] only focused on the bulk compensation but ignored the spatially variant components of LF errors. To deal with this issue, Chen et al. [23] and Zhang et al. [24] proposed LF error estimation and compensation methods based on the improved phase gradient autofocus (PGA) and the range-dependent map-drift algorithm (RDMDA), respectively. In both methods, the phase errors caused by spatially variant LF errors can be well removed. Meanwhile, Aye et al. [25] and Chen et al. [26] presented improved two-step MoCo methods based on motion data, which also took into account the spatially variant components of LF errors. However, all the abovementioned MoCo schemes cannot completely remove the influence of envelope spatial variations on imaging results, making them unsuitable for multirotor UAV SAR with large LF errors.

For HF errors, due to their distinct forms and characteristics, their impacts on imaging results are different from LF errors, making most conventional MoCo methods invalid. Fornaro [27] discussed the data spectrum with both linear and HF sinusoidal trajectories according to the geometric model and his analytical results can effectively evaluate the impacts of HF errors on imaging qualities. Zhang et al. [28] proposed an HF vibration compensation method for THz-SAR that can correct the ranging cell migrations caused by HF errors through the successive Doppler keystone transform (SDKT). Gao et al. [29] estimated the vibration frequency through the extracted HF phase errors and then suppressed the HF phase errors. Qu et al. [30] developed an HF error estimation method based on piecewise fast Fourier transform (FFT), which can determine the HF error parameters and ultimately realize HF error compensation. However, most of them can only accurately estimate and compensate for the single-component HF errors, which perform poorly for multirotor UAV SAR.

In this article, a geometric model of multirotor UAV SAR is established, which divides the complex range history into different parts and the influence of them on imaging quality is analyzed in detail. Our analysis shows that both the phase and envelope spatial variations caused by LF errors would significantly degrade imaging quality and the presence of HF errors would introduce pairs of ghosts around the target. To address these problems separately, an improved two-step MoCo method based on scaling correction is devised to effectively remove the LF
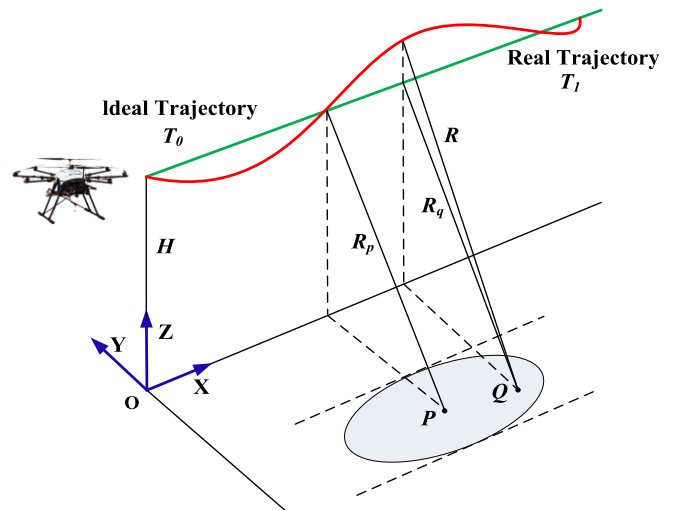

Fig. 2. Multirotor UAV SAR imaging geometry model with motion errors.

errors and an extended PGA scheme is introduced to compensate for the HF errors. Unlike the traditional MoCo methods, our approach can effectively remove LF and HF errors step-by-step with high robustness, which is suitable for multirotor UAV SAR.

The rest of this article is organized as follows. In Section II, the geometric model of the multirotor UAV SAR with complex motion errors is established, and the effects of LF and HF errors are analyzed. In Section III, an improved two-step MoCo method based on scaling correction is proposed for LF errors and an extended PGA scheme is introduced for HF errors. Discussions are given in Section IV. Numerical results from computer simulation and real data experiment are provided in Section V. Finally, Section VI concludes this article.

II. MODELING

In this section, the imaging geometry of multirotor UAV SAR is established, which takes into account arbitrary targets in the imaging scene. Based on our geometric model, the influence of both LF and HF errors on imaging results is then analyzed in detail.

A. Geometric Model

The 3-D rectangular coordinate system is employed to describe the geometric model of multirotor UAV SAR with motion errors, as shown in Fig. 2. Here, O is the origin of the Cartesian coordinates $o\text{-}xyz$. The platform is assumed to fly along the x-axis direction with average velocity v and altitude H. The ideal and real flight trajectories of the platform are denoted as T_0 (green solid line) and T_1 (red solid line), respectively, and the coordinates are denoted as $[v\eta, 0, H]$ and $[X(\eta), Y(\eta), Z(\eta)]$, where η is the azimuth slow time. P and Q are the central reference and arbitrary targets on the ground scene, respectively. R_p and R_q represent the closest slant ranges from targets P and Q, respectively, to the ideal flight trajectory. According to the geometric model, the true instantaneous slant range history $R(\eta)$

of Q is expressed as

$$R(\eta) = \sqrt{[X(\eta) - X_q]^2 + [Y(\eta) - Y_q]^2 + [Z(\eta) - Z_q]^2} \quad (1)$$

where $[X_q, Y_q, Z_q]$ represents the coordinates of Q. Then, let the motion errors along the x-axis, y-axis, and z-axis be $\Delta X(\eta)$, $\Delta Y(\eta)$ and $\Delta Z(\eta)$, respectively, the instantaneous slant range history in (1) can be approximated by the Taylor series as

$$
\begin{aligned}
R(\eta) &\\
&\approx \sqrt{[V\eta + \Delta X(\eta) - X_q]^2 + [\Delta Y(\eta) - Y_q]^2 + [H + \Delta Z(\eta)]^2} \\
&\approx R_q + \frac{(V\eta + \Delta X(\eta) - X_q)^2}{2R_q} \\
&\quad - \frac{Y_q}{R_q}\Delta Y(\eta) + \frac{H}{R_q}\Delta Z(\eta) \\
&= R_q + \frac{(V\eta + \Delta X(\eta) - X_q)^2}{2R_q} \\
&\quad - \Delta Y(\eta)\sin\theta_q + \Delta Z(\eta)\cos\theta_q \quad (2)
\end{aligned}
$$

where θ_q denotes the incident angle of the target, and R_q is the closet slant range from Q to the ideal flight trajectory, i.e., $R_q = \sqrt{Y_q{}^2 + H^2}$.

Generally, motion errors are divided into two components: along-track errors determined by $\Delta X(\eta)$ and cross-track errors determined by $\Delta Y(\eta)$ and $\Delta Z(\eta)$. For the former, they are usually caused by variations in the forward velocity, which can be effectively removed by adjusting the pulse repetition frequency (PRF) or performing phase error estimation [31], and thus, only the cross-track errors are analyzed in this section. For multirotor UAVs, due to their complicated motion form and flight characteristics, the cross-track errors are composed of both LF and HF errors. To accurately evaluate their impacts on imaging qualities, the instantaneous slant range history in (2) can then be rewritten as

$$R(\eta) = R_0(\eta) + \Delta R_{at}(\eta) + \Delta R_{low}(\eta) + \Delta R_{high}(\eta) \quad (3)$$

where

$$R_0(\eta) = R_q + \frac{(V\eta - X_q)^2}{2R_q} \quad (4)$$

$$\Delta R_{at}(\eta) = \frac{\Delta X(\eta)^2 + 2\Delta X(\eta)(V\eta - X_q)}{2R_q} \quad (5)$$

$$\Delta R_{low}(\eta) = -\Delta Y_{low}(\eta)\sin\theta_q + \Delta Z_{low}(\eta)\cos\theta_q \quad (6)$$

$$\Delta R_{high}(\eta) = -\Delta Y_{high}(\eta)\sin\theta_q + \Delta Z_{high}(\eta)\cos\theta_q. \quad (7)$$

Here, $R_0(\eta)$ is the expected range history, $\Delta R_{at}(\eta)$ is the along-track errors, $\Delta R_{low}(\eta)$ and $\Delta R_{high}(\eta)$ denote the cross-track LF and HF errors, respectively, and we write LF and HF errors for short in the manuscript. $\Delta Y_{low}(\eta)$ and $\Delta Z_{low}(\eta)$ are the LF errors along y-axis and z-axis, respectively, while $\Delta Y_{high}(\eta)$ and $\Delta Z_{high}(\eta)$ are the corresponding HF errors.
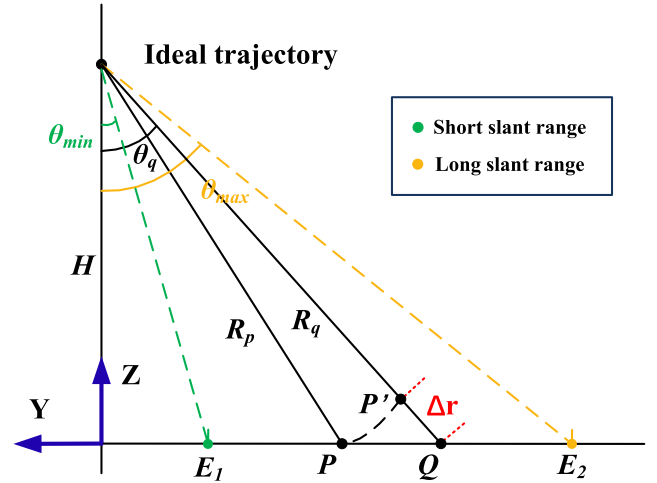

Fig. 3.   Side view of multirotor UAV SAR imaging geometry.

B. Low-Frequency Error Analyses

Compared to traditional aircraft, it is more susceptible to atmospheric turbulence due to its small size and light weight for multirotor UAV, introducing larger LF errors. In this case, the impacts of the spatial variation in LF errors on imaging results would also become more severe.

To better analyze the impacts of spatially variant LF errors on imaging quality, $\cos\theta_q$ and $\sin\theta_q$ in (6) are expanded as

$$
\begin{aligned}
\cos\theta_q &= \frac{H}{R_p + \Delta r} \\
&\approx \sum_{n=0} C_i(H, R_p)\Delta r^n \\
&\approx \frac{H}{R_p} - \frac{H}{R_p^2}\Delta r + \sum_{n=2} C_i(H, R_p)\Delta r^n
\end{aligned}
$$

$$
\begin{aligned}
\sin\theta_q &= \left[1 - \frac{H^2}{(R_p + \Delta r)^2}\right]^{1/2} \\
&\approx \sum_{n=0} D_i(H, R_p)\Delta r^n \\
&\approx \left(\frac{R_p^2 - H^2}{R_p^2}\right)^{1/2} + \left(\frac{R_p^2 - H^2}{R_p^2}\right)^{1/2} \\
&\quad \times \frac{H^2}{R_p(R_p^2 - H^2)}\Delta r + \sum_{n=2} D_i(H, R_p)\Delta r^n \quad (8)
\end{aligned}
$$

where $R_q = R_p + \Delta r$ with Δr being the slant range from P to Q, as shown in Fig. 3. C_0 and D_0 are the spatially invariant component coefficients of LF errors. C_i and D_i denote the ith order spatially variant component coefficients of LF errors.

Generally, both the envelope and phase errors would be introduced into the echo signal by spatially variant LF errors. To evaluate the impacts of different order spatially variant components of LF errors on imaging results separately, a set of computer simulations is conducted here. The main radar
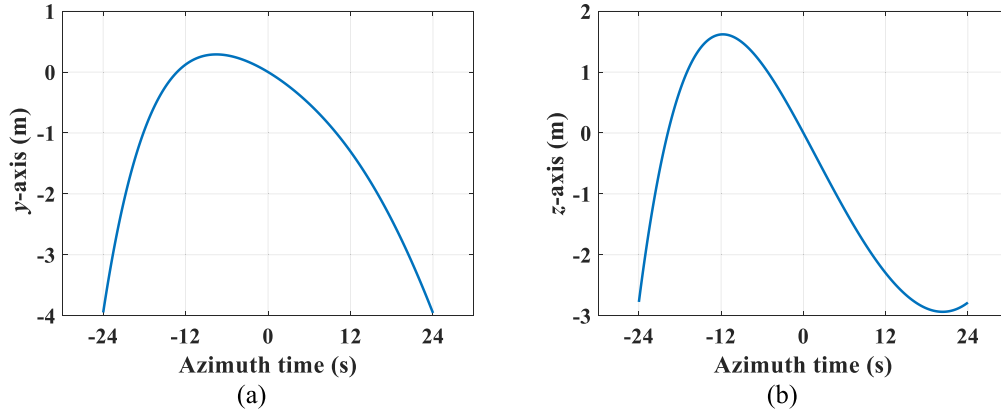
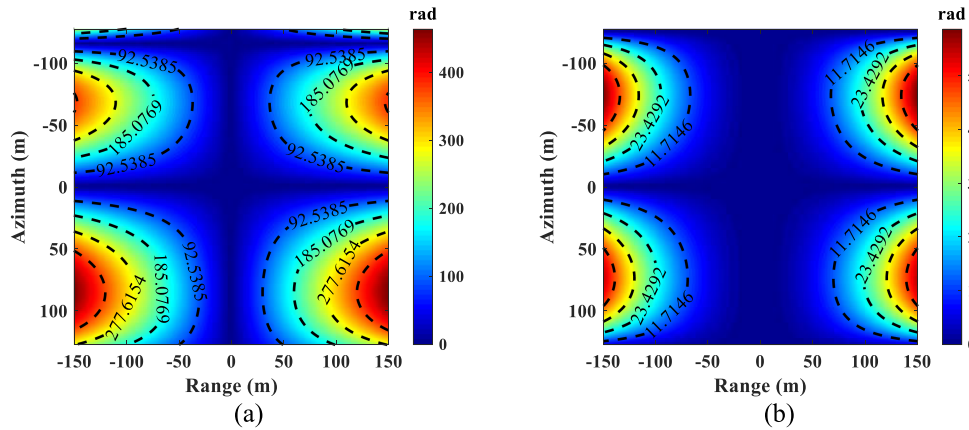Fig. 4. LF errors of multirotor UAV platform (a) y-axis. (b) z-axis.

Fig. 5. Phase errors induced by spatially variant LF errors with different orders. (a) First-order spatially variant component. (b) High-order spatially variant components.

TABLE I
SYSTEM PARAMETERS

System parameter	Value
Carrier frequency	9.6 GHz
Transmitted bandwidth	750 MHz
Sampling frequency	800 MHz
Pulse repetition frequency	333 Hz
Squint angle	0°
Central slant range	1200 m
Platform height	300 m
Platform speed	5 m/s

system parameters are listed in Table I. The platform is assumed to fly along the x-axis with an average velocity 5 m/s. Fig. 4 plots the simulated LF errors along the y-axis and z-axis of the platform. The central slant range and average altitude are 1200 and 300 m, respectively. The simulated imaging scene dimensions are 300 m × 240 m (range × azimuth) with incident angle ranges from $\theta_{\min} = 73°$ to $\theta_{\max} = 77°$, as shown in Fig. 3, where E_1 and E_2 indicate the edge points of the scene. Multiple point targets are set at intervals of 0.1 m in both distance and

azimuth directions in the imaging scene. Then, based on the motion errors in Fig. 4 and the parameters in Table I, we calculate the phase and envelope errors caused by different order spatially variant components for each point in the imaging scene. The results are plotted in Figs. 5 and 6, where the horizontal and vertical coordinates represent the positions of range and azimuth in the imaging scene, respectively.

Fig. 5(a) and (b) plots the phase errors caused by the first-order and high-order spatially variant components of LF errors, respectively. The unit of the contour map is radian (rad). It is seen that the maximum phase errors caused by them are approximately 455 and 56 rad, respectively. Obviously, both of them are greater than $\pi/4$, and thus, cannot be ignored for multirotor UAV SAR [32], [33]. Moreover, Fig. 6(a) and (b) plots the envelope errors, respectively, caused by the first-order and high-order spatially variant components of LF errors. The unit of the contour map is meter (m). One can see that the maximum envelope errors introduced by the first-order spatially variant component are approximately 0.5 m, which are greater than 0.5 range unit, and the maximum envelope errors introduced by high-order spatially variant components are about 0.04 m, which are far less than 0.5 range unit. Here, the range unit is 0.1875 m, which is determined by the sampling frequency.
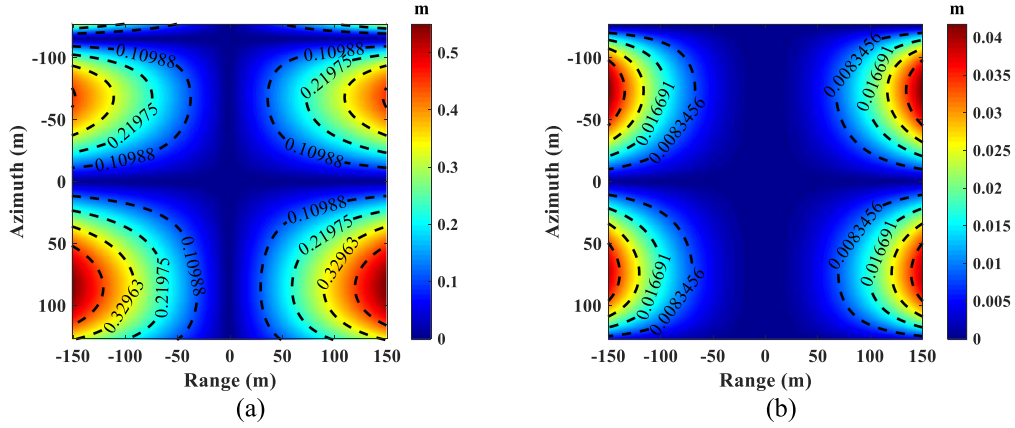
Fig. 6.   Envelope errors induced by spatially variant LF errors with different orders. (a) First-order spatially variant component. (b) High-order spatially variant components.

Therefore, for multirotor UAV SAR, the envelope errors caused by the high-order spatially variant components can be neglected but not the first-order spatially variant components in most flight conditions [4], [32].

Considering various impacts of the different order spatially variant components of LF errors on imaging results, the LF errors can be separated into three parts

$$\Delta R_{\text{low}}(\eta) = \Delta R_{\text{low\_0}}(\eta) + \Delta R_{\text{low\_1}}(\eta) + \Delta R_{\text{low\_h}}(\eta) \quad (9)$$

where $\Delta R_{\text{low\_0}}(\eta)$ represents the bulk component (i.e., spatially invariant component) of LF errors. $\Delta R_{\text{low\_1}}(\eta)$ and $\Delta R_{\text{low\_h}}(\eta)$ are the first-order and high-order spatially variant components of LF errors, respectively. Clearly, these three components need to be removed in different ways in subsequent algorithm design.

C. High-Frequency Error Analyses

Unlike traditional aircraft, the motion state of multirotor UAV is affected by the rotation of the propellers, introducing HF errors. Compared with LF errors, HF errors have different forms and characteristics. To better analyze their impacts on imaging results, the *sinusoidal* resonance model is used here to describe the HF error component [16], [19], and (7) can then be rewritten as

$$\Delta R_{\text{high}}(\eta) = \sum_{i=1}^{M_1} a_i \sin(2\pi f_i \eta) \sin\theta_q$$
$$+ \sum_{i=1}^{M_2} a_i \sin(2\pi f_i \eta) \cos\theta_q$$
$$= \sum_{i=1}^{M} A_i \sin(2\pi f_i \eta) \quad (10)$$

where M is the number of the HF error components. A_i and f_i are, respectively, the equivalent amplitude and frequency of the ith HF error component. Generally, the average amplitude of the HF errors is only a few millimeters, far less than 0.5 range unit, and their resulting envelope errors can be ignored [20], [34]. Therefore, only the phase errors introduced by HF errors

are analyzed here, which can be expressed as

$$\Delta\varphi_{\text{high}}(\eta) = \exp\left\{-j\frac{4\pi}{\lambda} \cdot \sum_{i=1}^{M} A_i \sin(2\pi f_i \eta)\right\} \quad (11)$$

where λ is the wavelength of the transmitted signal.

To facilitate a better understanding of the additional HF phase errors, (11) can be expanded by the first kind of Bessel function as

$$\Delta\varphi_{\text{h}}(\eta)$$
$$= \prod_{i=1}^{M}\left\{J_0(z_i) + \sum_{k=1}^{+\infty} j^k J_k(z_i)\cos\left(2\pi k f_i \eta - \frac{\pi k}{2}\right)\right\} \quad (12)$$

where

$$z_i = -\frac{4\pi}{\lambda} \cdot A_i. \quad (13)$$

Here, $J_k(z_i)$ is the kth order first kind of *Bessel* function with respect to z_i. Based on the properties of the coefficients of the Bessel functions [27], it is seen that due to the effects of the term $J_0(z_i)$ on echo signal, the energy of the desired target would be attenuated, and because of the effects of the term $J_k(z_i)\cos(2\pi k f_i \eta - \pi k/2)$ on echo signal, the paired false targets would be introduced. In addition to the parameters of HF error components, the degree of the expected target energy attenuation and the number of the introduced false targets are more susceptible to the number of HF error components.

To verify the above analysis, a set of computer simulations is conducted. Here, we set $M = 2$, where the two simulated HF error components are added along the y-axis and z-axis, respectively, as shown in Fig. 7. The main parameters of the radar are listed in Table I. The platform is assumed to fly along the x-axis with an average velocity 5 m/s. The central slant range and average altitude are 1200 and 300 m, respectively. The simulated scene dimensions are 300 m × 240 m (range × azimuth) with incident angle ranges from 73° to 77°. Based on the HF errors in Fig. 7 and the parameters in Table I, we plot the impulse

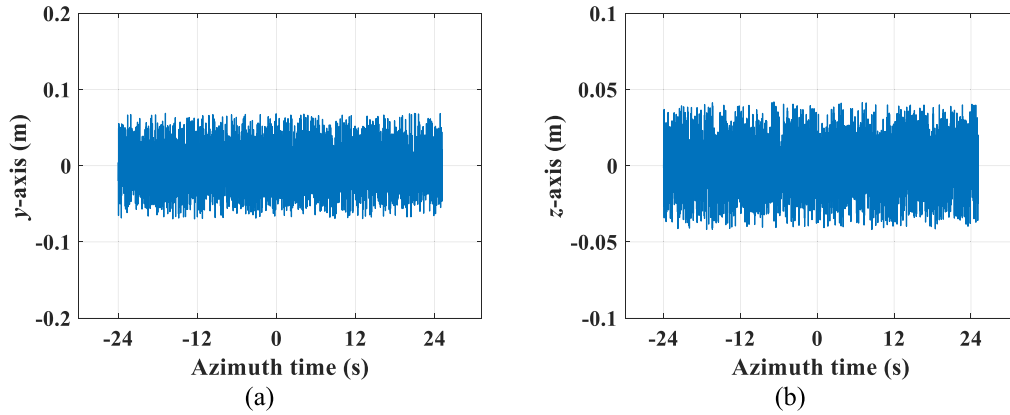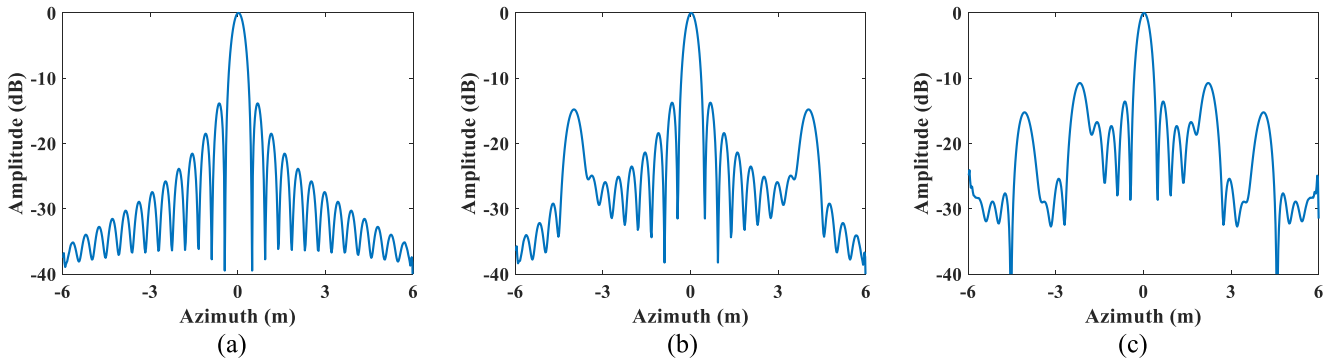Fig. 7. HF errors of multirotor UAV platform. (a) *y*-axis. (b) *z*-axis.

Fig. 8. Impulse responses of desired target after focusing. (a) Without HF errors. (b) With single-component HF errors. (c) With multiple-component HF errors.
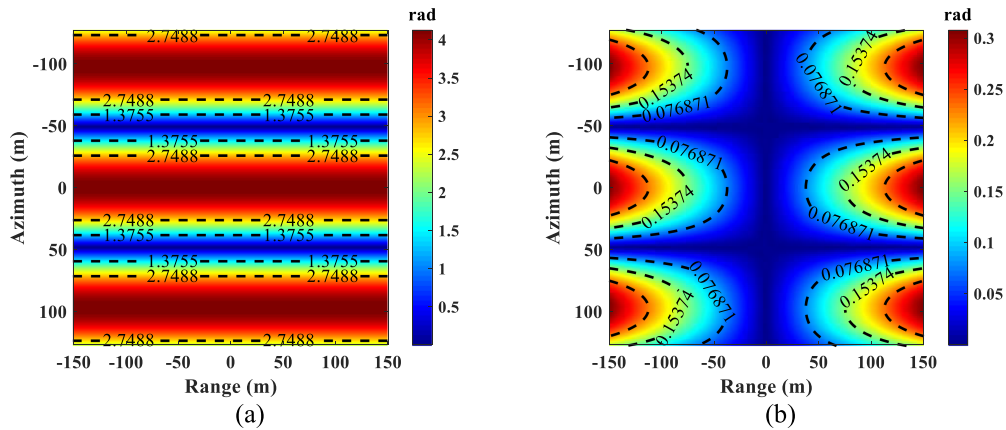

Fig. 9. Phase errors induced by HF errors with different components. (a) Bulk component. (b) Spatially variant component.

responses of the target at the edge of scene after preliminary focusing. Fig. 8(a) plots the result without the addition of HF errors for comparison. Fig. 8(b) shows the simulated results only with the addition of HF errors along the *y*-axis (i.e., single-component HF errors), while Fig. 8(c) plots the simulated results with the addition of HF errors along both the *y*-axis and *z*-axis (i.e., multiple-component HF errors). Clearly, side-lobes of the target are raised and grating-lobes are introduced around the target in

the presence of HF errors. Moreover, the degree of side-lobes increases and the number of grating-lobes is largely influenced by the number of HF error components, which corroborates the derivation in (12), indicating that the multiple-component HF errors cannot be ignored for multirotor UAV SAR imaging.

Furthermore, Fig. 9(a) and (b) plots the phase errors introduced by the bulk and spatially variant components of multiple-component HF errors, respectively. We observe that the

maximum phase errors caused by the bulk HF errors are greater than $\pi/4$, thus providing further validation for the necessity of HF error removal [32], [33]. Moreover, it is seen that under the parameter settings aligned with a real multirotor UAV SAR system, the maximum phase errors caused by the spatially variant components of HF errors are far less than $\pi/4$, which do not affect the imaging quality. Therefore, the HF errors can be considered as a bulk component for most application scenarios of multirotor UAV SAR, providing convenience for subsequent algorithm design.

D. Echo Signal

Suppose that the radar transmits a linear frequency modulation signal. According to the geometric model in Fig. 2, the echo signal of the arbitrary target Q in range time and azimuth time domain can be expressed as

$$S_0(\tau, \eta) = w_r(\tau)\, w_a(\eta) \exp\left[-j\frac{4\pi f_0 R(\eta)}{c}\right]$$
$$\cdot \exp\left[j\pi K_r\left(\tau - \frac{2R(\eta)}{c}\right)^2\right] \tag{14}$$

where τ is the range time, c is the speed of light, f_0 is the carrier frequency, and K_r is the *chirp* rate of transmitted signal. $w_r(\cdot)$ and $w_a(\cdot)$ are the envelopes in the range time domain and azimuth time domain, respectively.

According to the previous analysis, the complex range history is decomposed into different parts consisting of the expected range history, along-track errors, LF errors, and HF errors. Then, by combining their respective effects on the echo signal, performing range compression, ignoring unimportant amplitude and substituting (3) and (9) into (14), the echo signal in range frequency and azimuth time domain is given by

$$S_0(f_\tau, \eta) = W_r(f_\tau)\, w_a(\eta) \exp\left\{-j\frac{4\pi}{\lambda}R_0(\eta)\right\}$$
$$\times \exp\left\{-j\frac{4\pi}{c}f_\tau R_0(\eta)\right\}$$
$$\cdot \exp\left\{-j\frac{4\pi}{\lambda}\Delta R_{at}(\eta)\right\} \exp\left\{-j\frac{4\pi}{\lambda}\Delta R_{high}(\eta)\right\}$$
$$\cdot \exp\left\{-j\frac{4\pi}{\lambda}\left[\Delta R_{low\_0}(\eta) + \Delta R_{low\_1}(\eta) + \Delta R_{low\_h}(\eta)\right]\right\}$$
$$\cdot \exp\left\{-j\frac{4\pi}{c}f_\tau\left[\Delta R_{low\_0}(\eta) + \Delta R_{low\_1}(\eta)\right]\right\} \tag{15}$$

where the first and second exponential terms represent the phase modulation and envelope migration of the expected range history, respectively. The third and fourth exponential terms indicate the phase errors caused by along-track errors and HF errors, respectively. The fifth and last exponential terms correspond to the phase and envelope errors introduced by LF errors, respectively. Clearly, the complex motion errors of multirotor UAV SAR are effectively separated in our model, thus can be compensated in different ways step-by-step.

III. APPROACH

Based on the above model and analysis, the improved MoCo approach is proposed for multirotor UAV SAR in this section. To greatly decrease the impacts of the complex motion errors on the imaging results, our approach is mainly divided into two steps. The first step, i.e., LF error compensation, is to eliminate the envelope and phase errors introduced by spatially variant LF errors. The second step, i.e., HF error compensation, aims to remove the phase errors caused by HF errors, which also cannot be ignored for multirotor UAV SAR.

A. Low-Frequency Error Compensation

Generally, the conventional two-step MoCo approach is used to remove the LF errors. However, due to the envelope errors introduced by the spatially variant components of LF errors, the performance of the conventional two-step MoCo approach would become unsatisfactory for multirotor UAV SAR, degrading imaging qualities. To solve this issue, an improved two-step MoCo approach is developed in this section to effectively remove the spatially variant LF errors for multirotor UAV SAR.

1) Scaling Correction: The first step of the improved MoCo aims to correct the spatially variant LF envelope errors (i.e., the envelope errors introduced by the spatially variant components of LF errors) which can be rewritten according to (8) as

$$\Delta R_{low\_1}(\eta)$$
$$= \frac{D_1(H, R_p)\,\Delta r \cdot \Delta Y_{low}(\eta) + C_1(H, R_p)\,\Delta r \cdot \Delta Z_{low}(\eta)}{D_0(H, R_p) \cdot \Delta Y_{low}(\eta) + C_0(H, R_p) \cdot \Delta Z_{low}(\eta)}$$
$$\cdot \Delta R_{low\_0}(\eta)$$
$$= \alpha(\eta) \cdot \Delta R_{low\_0}(\eta) \tag{16}$$

where α represents the linear coefficient of LF envelope errors. Unlike the expected slant range history, the motion errors are random, indicating that the variation of the linear coefficient versus azimuth time is unpredictable, making it impossible to design a unified compensation function for spatially variant LF envelope errors. Consequently, the scaling correction of the echo signal is performed here through chirp-z transform (CZT), to remove the spatially variant LF envelope error, where the detailed derivation is provided in Appendix A. Then, the echo signal in (15) can be rewritten as

$$S_0(f'_\tau, \eta) = W_r(f'_\tau)\, w_a(\eta) \exp\left\{-j\frac{4\pi}{\lambda}R_0(\eta)\right\}$$
$$\cdot \exp\left\{-j\frac{4\pi}{\lambda}\Delta R_{at}(\eta)\right\} \exp\left\{-j\frac{4\pi}{\lambda}\Delta R_{high}(\eta)\right\}$$
$$\cdot \exp\left\{-j\frac{4\pi}{\lambda}\left[\Delta R_{low\_0}(\eta) + \Delta R_{low\_1}(\eta) + \Delta R_{low\_h}(\eta)\right]\right\}$$
$$\cdot \exp\left\{-j2\pi f'_\tau \frac{2\left[R_0(\eta) + \Delta R_{low\_0}(\eta) + \Delta R_{low\_1}(\eta)\right]}{[1 + \alpha(\eta)]\,c}\right\}. \tag{17}$$
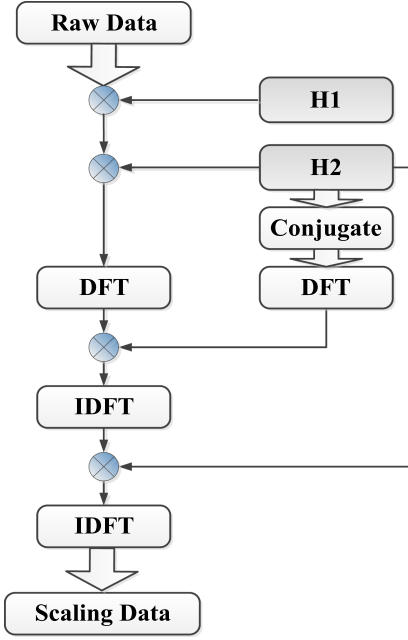
Fig. 10.   Flowchart of scaling correction.

For ease of presentation, f'_τ is still expressed as f_τ below. Then, by substituting (16) into (17), one obtains

$$S_0\left(f_\tau,\eta\right) = W_r\left(f_\tau\right)w_a(\eta)\exp\left\{-j\frac{4\pi}{\lambda}R_0(\eta)\right\}$$

$$\cdot \exp\left\{-j\frac{4\pi}{\lambda}\Delta R_{at}(\eta)\right\}\exp\left\{-j\frac{4\pi}{\lambda}\Delta R_{high}(\eta)\right\}$$

$$\cdot \exp\left\{-j\frac{4\pi}{\lambda}\left[\Delta R_{low\_0}(\eta)+\Delta R_{low\_1}(\eta)+\Delta R_{low\_h}(\eta)\right]\right\}$$

$$\cdot \exp\left\{-j2\pi f_\tau\frac{2\Delta R_{low\_0}(\eta)}{c}\right\}$$

$$\cdot \exp\left\{-j2\pi f_\tau\frac{2R_0(\eta)}{[1+\alpha(\eta)]c}\right\}. \tag{18}$$

Apparently, the spatially variant LF envelope errors are effectively removed through scaling correction. To facilitate a better understanding, the flowchart of scaling correction is shown in Fig. 10, where the two functions H_1 and H_2 are

$$H_1(\tau,\eta) = \exp\left\{j\pi\left(1+\alpha\right)\frac{\tau}{\Delta T}\right\} \tag{19}$$

$$H_2(\tau,\eta) = \exp\left\{-j\pi\frac{1}{N}\left(1+\alpha\right)\left(\frac{\tau}{\Delta T}\right)^2\right\} \tag{20}$$

with N being the range cell number and ΔT being the sampling interval in range time dimension.

2) Two-Step MoCo: After scaling correction, the conventional two-step MoCo approach is employed to compensate for the bulk LF phase and envelope errors as well as spatially variant LF phase errors. Generally, the envelop errors are compensated in the range frequency and azimuth time domain, and the phase errors are compensated in range time and azimuth time

domain [31]. Among them, the first-step MoCo is employed to remove the bulk LF errors, where the compensation function is expressed as

$$H_3\left(f_\tau,\eta\right) = \exp\left[j\frac{4\pi\left(f_0+f_\tau\right)}{c}\Delta R_{low\_0}(\eta)\right]. \tag{21}$$

Then, the second-step MoCo compensates for the spatially variant LF phase errors with compensation function

$$H_4(\tau,\eta) = \exp\left\{j\frac{4\pi}{\lambda}\left[\Delta R_{low\_1}(\eta)+\Delta R_{low\_h}(\eta)\right]\right\} \tag{22}$$

where λ is the wavelength of transmitted signal. Due to the significant impacts of the bulk errors on the echo signal, the first-step MoCo is usually performed prior to ranging cell migration correction (RCMC), while the second-step MoCo follows RCMC [31], [35].

3) Additional Error Correction: After RCMC and two-step MoCo, the LF errors are basically eliminated and the echo signal in (18) becomes

$$S_0\left(f_\tau,\eta\right) = W_r\left(f_\tau\right)w_a(\eta)\exp\left\{-j\frac{4\pi}{\lambda}R_0(\eta)\right\}$$

$$\times \exp\left\{-j2\pi f_\tau\frac{2R_q}{c}\right\}$$

$$\cdot \exp\left\{-j\frac{4\pi}{\lambda}\Delta R_{at}(\eta)\right\}\exp\left\{-j\frac{4\pi}{\lambda}\Delta R_{high}(\eta)\right\}$$

$$\cdot \exp\left\{j2\pi f_\tau\frac{2\alpha(\eta)}{[1+\alpha(\eta)]c}R_0(\eta)\right\}. \tag{23}$$

According to (23), it is seen that the additional envelope errors introduced by scaling correction still remain in the echo signal. These errors will be analyzed in detail in Section IV. Generally, the additional envelope errors can be considered as spatially invariant [26], which are approximated according to (4) as

$$E\left(f_\tau,\eta\right) = \exp\left\{j\frac{4\pi f_\tau}{c}\frac{\alpha(\eta)}{[1+\alpha(\eta)]}\left[R_p+\frac{(V\eta)^2}{2R_p}\right]\right\}. \tag{24}$$

Based on the principle of stationary phase (POSP), the compensation function in 2-D frequency domain for additional envelope errors can be accordingly constructed as

$$H_{add}\left(f_\tau,f_\eta\right) = \exp\left\{j\frac{4\pi f_\tau R_p}{c}\frac{\alpha\left(f_\eta\right)}{[1+\alpha\left(f_\eta\right)]}\left(\frac{8V+\lambda^2 f_\eta^2}{8V}\right)\right\} \tag{25}$$

where f_η represents the azimuth frequency.

B. High-Frequency Error Compensation

After LF error compensation, the echo signal in range time and azimuth time domain can be expressed as

$$S_0(\tau,\eta) = w_r\left\{\tau-\frac{2R_q}{c}\right\}w_a(\eta)\exp\left\{-j\frac{4\pi}{\lambda}R_0(\eta)\right\}$$

$$\cdot \exp\left\{-j\frac{4\pi}{\lambda}\Delta R_{at}(\eta)\right\}\exp\left\{-j\frac{4\pi}{\lambda}\Delta R_{high}(\eta)\right\}. \tag{26}$$

Apparently, the HF phase errors still exist in the echo signal. However, due to their different forms and characteristics, it is difficult to compensate for the HF errors through conventional MoCo methods. In this subsection, an extended phase gradient autofocus (PGA) scheme is introduced to realize the estimation and correction of HF errors.

The principle of PGA is to make an optimal estimation of the phase error gradient through the defocused SAR image. The estimation process only exploits the redundant information of the strong scattering points in the degraded SAR image, independent of the imaging scene content [36], [37]. Therefore, PGA can achieve accurate estimation of random phase errors without relying on any prior information about the error, such as frequency and amplitude, which can effectively avoid the impacts of multicomponent coupling on the accuracy of parameter estimation, making it suitable for multicomponent HF phase error compensation. Here, based on the characteristics of HF errors, several significant extensions are made to the traditional PGA methodology to enhance HF error estimation.

1) First, the bulk LF phase errors compensated previously can be re-added to the echo signal prior to estimating the HF phase errors. In this way, the grating-lobes resulting from HF errors can be submerged within the degraded side-lobes of the target caused by LF errors [38], enabling accurate acquisition of the target position through circular shifting and windowing. Otherwise, the grating-lobes may be mistaken for the real targets, resulting in significant estimation errors. After completion of the estimation procedure, the required HF phase errors can be determined by removing the added LF phase errors from the estimated result for subsequent processing.

2) Second, the echo signal can be divided into several range blocks, and only those with enough strong scattering points are chosen for HF phase error estimation. Since the HF errors can be considered as a bulk component, the estimated results of each selected range block are all for precompensation, and only the ones with the best compensation effect is selected as the desired result. Particularly, the precompensation effect can be evaluated by the entropy of the compensated image, where lower entropy indicates better effect [23].

After HF phase error estimation through the extended PGA, the HF error compensation function can be constructed as

$$H_f(\tau, \eta) = \exp\{j\varphi_h(\eta)\} \qquad (27)$$

where $\varphi_h(\eta)$ denotes the estimated HF phase errors.

By multiplying (27) by (26), the HF errors are effectively corrected, and the echo signal can then be expressed as

$$S_0(\tau, \eta) = w_r\left\{\tau - \frac{2R_q}{c}\right\} w_a(\eta) \exp\left\{-j\frac{4\pi}{\lambda}R_0(\eta)\right\}$$
$$\cdot \exp\left\{-j\frac{4\pi}{\lambda}\Delta R_{\text{at}}(\eta)\right\}. \qquad (28)$$

Compared to the traditional PGA methodology, our scheme is more suitable for HF error correction with high accuracy and robustness. Subsequently, a method based on parameter estimation [31] can be applied to eliminate the along-track errors. First, the
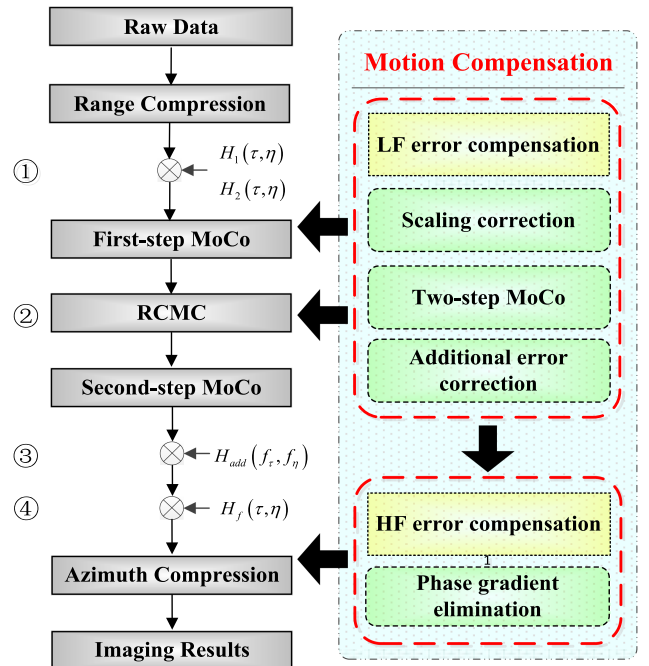

Fig. 11.   Flowchart of imaging approach.

modified map drift (MD) algorithm is employed to estimate the Doppler rate error $\Delta\gamma(\eta)$ caused by along-track errors. Then, the corresponding phase perturbation $\Delta\varphi_{\text{at}}(\eta)$ is calculated by double integral of $\Delta\gamma(\eta)$. Finally, $\Delta\varphi_{\text{at}}(\eta)$ is subtracted from the echo signal and azimuth distortion correction is performed to remove the influence of along-track errors, ultimately achieving high-resolution imaging of multirotor UAV SAR.

C. Flowchart of Imaging Approach

The flowchart of the imaging approach with the improved MoCo is depicted in Fig. 11. Note that the proposed approach is divided into two steps, i.e., LF error compensation and HF error compensation, which can be effectively combined with various imaging algorithms. The main procedure of the improved MoCo approach is described as follows.

1) Scaling correction: Eliminate the spatially variant LF envelope errors through scaling correction of echo signals based on the designed CZT function.

2) Two-step MoCo: Compensate for the bulk LF phase and envelope errors through the first-step MoCo, and for the spatially variant LF phase errors by the second-step MoCo.

3) Additional error correction: Remove the additional envelope errors introduced by scaling correction, which cannot be ignored for high-resolution multirotor UAV SAR.

4) HF error correction: Estimate and correct the HF phase errors through extended PGA scheme.

IV. DISCUSSION

A. Additional Envelop Errors

According to (23), the additional envelope errors induced by scaling correction are mainly affected by α. To analyze the magnitude of the introduced additional envelope errors,
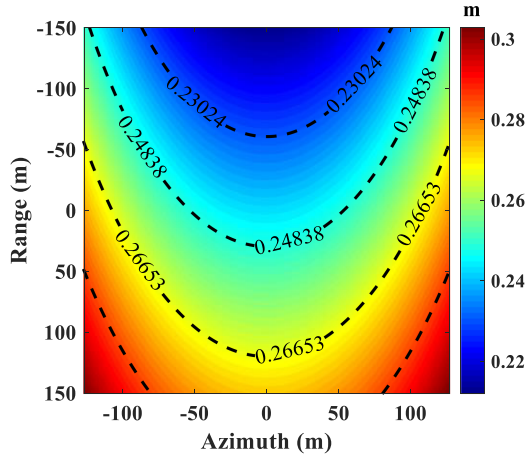
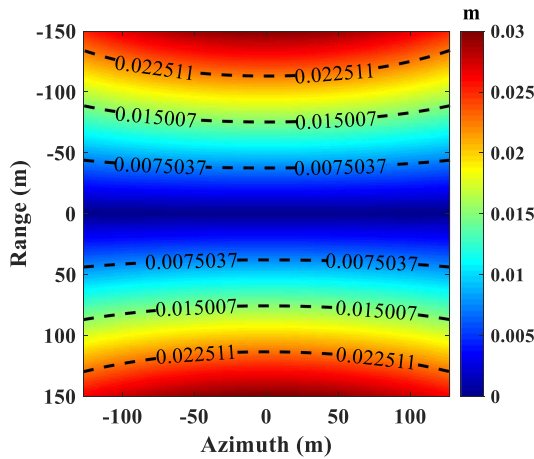Fig. 12. Additional envelope errors indured by scaling correction.

Fig. 13. Spatially variant components of additional envelope errors.

a set of computer simulations is conducted. The main radar system parameters are listed in Table I. The simulated imaging scene dimensions are 300 m × 240 m (range × azimuth). The simulated motion errors are shown in Fig. 4, and $\alpha = 0.0002$ is calculated according to (8) and (16). We then plot the additional envelope errors for each point in the scene, as shown in Fig. 12. The unit of the contour map is meter (m). It is clear that the maximum additional envelope errors are greater than 0.5 range unit, and thus, cannot be neglected for multirotor UAV SAR. Moreover, Fig. 13 plots the spatially variant components of additional envelope errors. It is observed that they are far less than 0.5 range unit. Therefore, the additional envelope errors can be considered as spatially invariant in subsequent processing.

V. NUMERICAL RESULTS

To evaluate the performance of the proposed approach, computer simulations and real data experiments are conducted in this section.

TABLE II
AZIMUTH IMAGE QUALITY PARAMETERS IN CASE I

Method	Target	IRW (m)	PSLR (dB)	ISLR (dB)
Without correction	P00	0.20	−13.82	−10.80
	P01	0.38	−5.43	−1.86
[26]	P00	0.20	−13.86	−10.85
	P01	0.23	−13.09	−9.98
Proposed	P00	0.20	−13.89	−10.91
	P01	0.20	−13.66	−10.79

A. Computer Simulations

Two sets of computer simulations are performed to evaluate the proposed approach. Case I considers the LF errors and Case II for the HF errors. The motion trajectory of the multirotor UAV platform with LF and HF errors in Cases I and II is shown in Figs. 14 and 15, respectively. The main radar acquisition parameters are listed in Table I. The scene dimensions are 300 m × 240 m (range × azimuth), with a dot array placed on the horizontal ground. As shown in Fig. 16, P00 is the target in the center of the ground scene, which can be used as a reference for comparison. The other four targets at the edge of the ground scene are denoted as P01, P02, P03, and P04, which are employed t for performance evaluation.

1) Case I: Fig. 17(a)–(c) shows the impulse response functions (IRFs) of the central reference target P00 focused without correction for the spatially variant components of LF errors, and with correction through the improved two-step MoCo approach [26] and the proposed approach, respectively. The azimuth profiles of P00 acquired by these three approaches are shown in Fig. 18. It is clear that they all effectively focus on the central reference target. For comparison, the IRFs of the scene edge target P01 processed by them are shown in Fig. 19(a)–(c), while Fig. 20 plots the corresponding azimuth profiles of P01. It is observed that the edge target is severely defocused without correcting the spatially variant components of LF errors. Moreover, the edge target is slightly defocused through [26], with main-lobe and side-lobes being coupled. This is because the additional envelop errors caused by scaling correction cannot be ignored for multirotor UAV SAR. The edge target can also be well focused by the proposed approach. In addition, the azimuth image quality parameters, including impulse response width (IRW), peak side-lobe ratio (PSLR), and integration side-lobe ratio (ISLR) are tabulated in Table II. Clearly, the image quality parameters of the proposed approach are close to the theoretical values, which demonstrate that the performance of the proposed approach is satisfactory for multirotor UAV SAR with large LF errors.

2) Case II: Fig. 21 plots the IRFs of P00 obtained without correction for HF errors, and with correction through traditional PGA [36] and the proposed approach, respectively. Fig. 22(a)–(c) plots the corresponding azimuth profiles of P00. For comparison, Fig. 23 shows the IRFs of P01 processed by different approaches, while Fig. 24 plots the corresponding azimuth profiles of P01. Note that the proposed approach focuses on all targets well, whereas [36] fails to do so. The main reason is
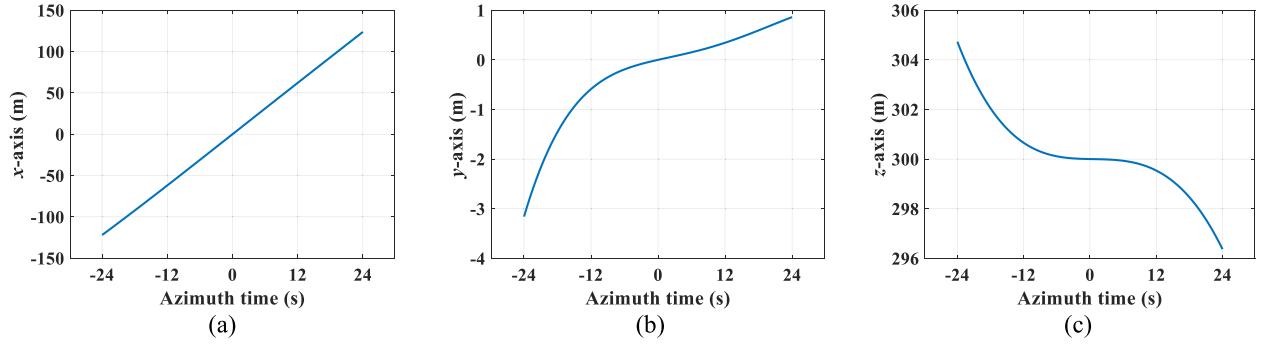
Fig. 14. Motion trajectory of multirotor UAV platform with LF errors. (a) *x*-axis. (b) *y*-axis. (c) *z*-axis.
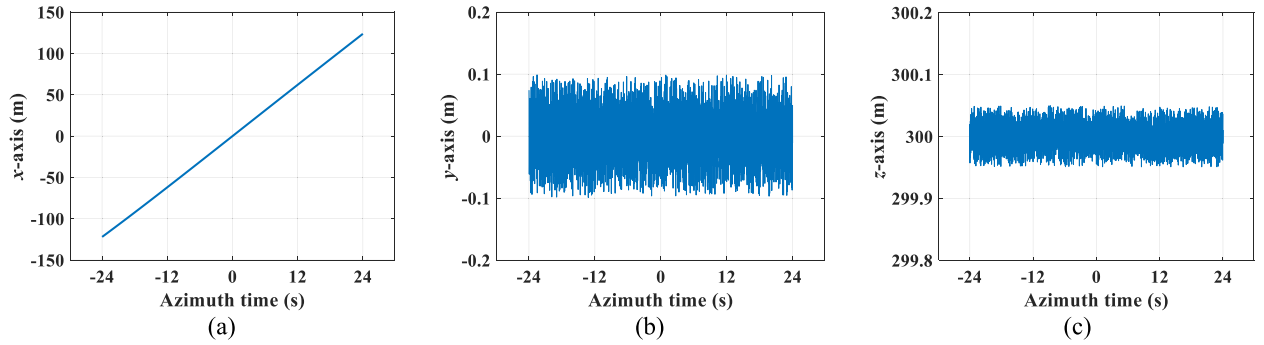

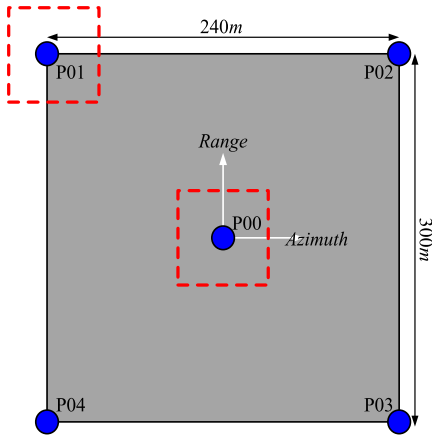Fig. 15. Motion trajectory of multirotor UAV platform with HF errors. (a) *x*-axis. (b) *y*-axis. (c) *z*-axis.

Fig. 16. Simulated scene.

TABLE III
AZIMUTH IMAGE QUALITY PARAMETERS IN CASE II

Method	Target	IRW (m)	PSLR (dB)	ISLR (dB)
Without correction	P00	0.22	−13.15	−3.15
	P01	0.23	−12.84	−3.09
[36]	P00	0.21	−13.31	−5.23
	P01	0.22	−12.96	−5.03
Proposed	P00	0.20	−13.89	−10.95
	P01	0.20	−13.48	−10.98

that, due to the characteristics of HF errors, the grating-lobes induced by HF errors are mistaken for the real targets [36], resulting in significant estimation errors. The azimuth image quality parameters for all approaches are listed in Table III. Apparently, the quality parameters of the proposed approach are superior to those of the remaining schemes, further validating the proposed approach in correcting HF errors.

B. Real Data Experiments

Two real data experiments are conducted to evaluate the proposed approach. Raw data were collected by a multirotor

UAV SAR system, which operates in the *X*-band with a carrier frequency of 9.6 GHz. The bandwidth and PRF of the transmitted signal are 750 MHz and 333 Hz, respectively. In Case I, the real data were collected on 27 November 2021, in Shijiazhuang City, Hebei Province, China, with the central slant range and height of the platform, respectively, being 1800 and 600 m, which are used to validate the performance of our approach to remove LF errors. In Case II, the real data were collected on 21 June 2021, in Leping City, Jiangxi Province, China, with the central slant range and height, respectively, being 600 and 300 m, aiming to illustrate the performance of our approach to suppress HF errors.

1) Case I: Fig. 25(a)–(c) plots the imaging results obtained without correction for the spatially variant components of LF errors, and with correction through [26] and the proposed approach, respectively. The edge scenes are extracted from the images to present the focusing details, as shown in Fig. 26. It is noted that the degraded side-lobes of the target caused by
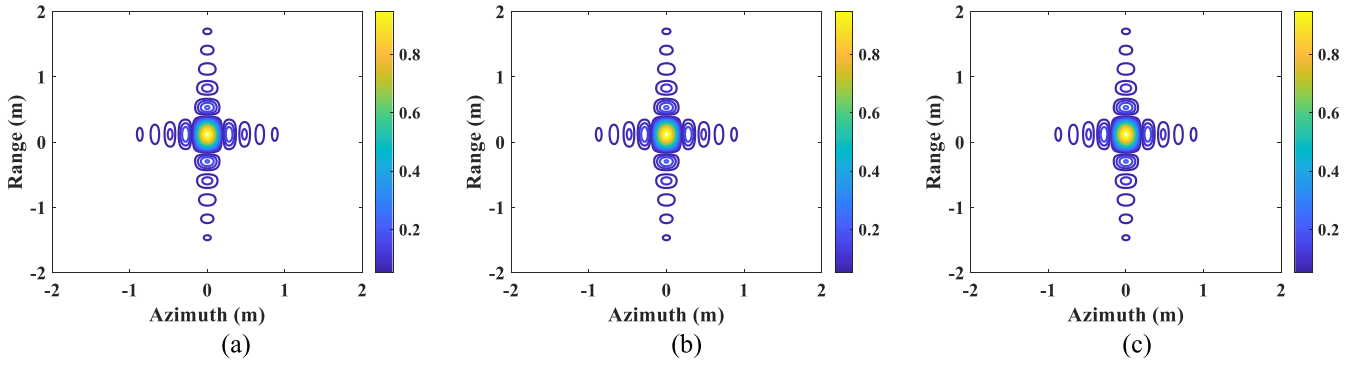
Fig. 17. 2-D IRFs of target P00. (a) Without correction. (b) [26]. (c) Proposed approach.
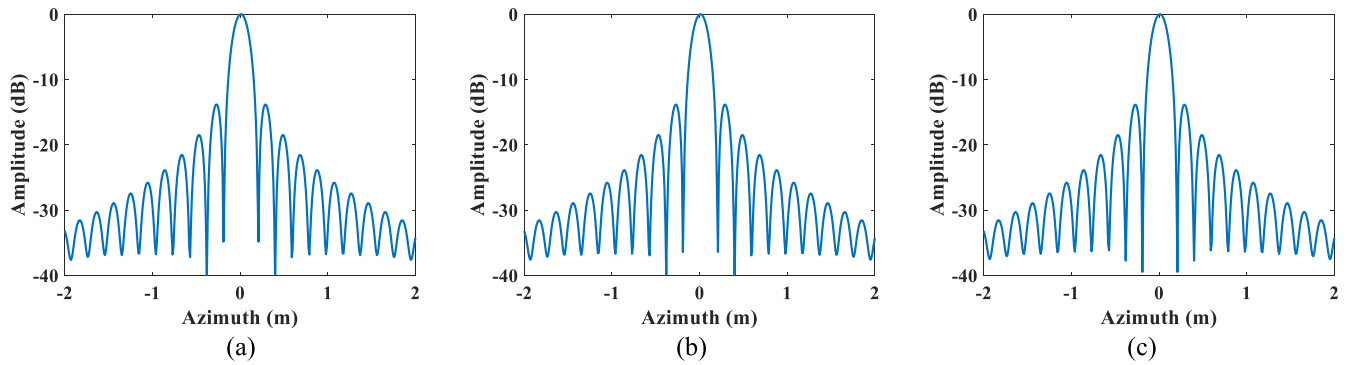

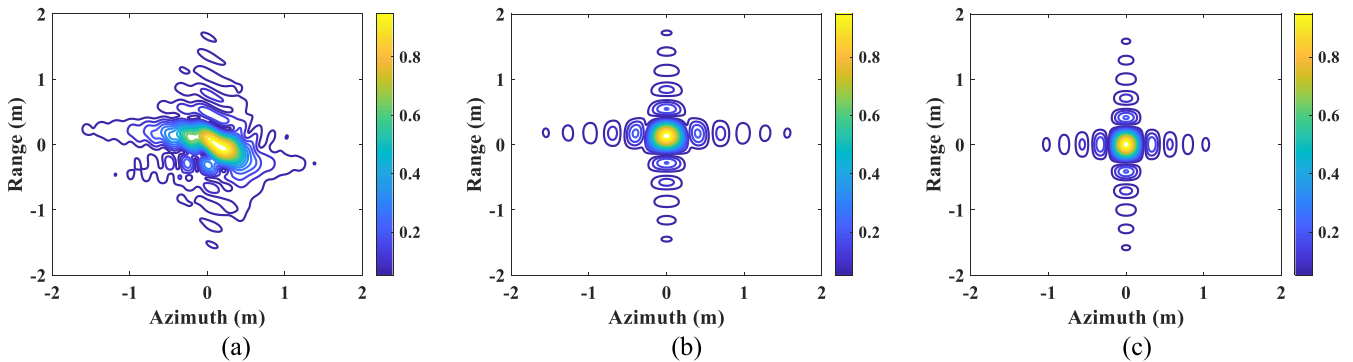Fig. 18. Azimuth profiles of target P00. (a) Without correction. (b) [26]. (c) Proposed approach.

Fig. 19. 2-D IRFs of target P01. (a) Without correction. (b) [26]. (c) Proposed approach.

TABLE IV
AZIMUTH IMAGE QUALITY PARAMETERS OF SELECTED TARGET IN CASE I

Method	IRW (m)	PSLR (dB)	ISLR (dB)
Without correction	0.41	−9.73	−9.18
[26]	0.25	−25.82	−19.62
Proposed	0.20	−29.41	−21.97

LF errors are well suppressed through our approach. Moreover, Fig. 27 plots the azimuth profiles of a selected scattering point in the edge scene acquired by different approaches and Table IV

lists their quality parameters. Apparently, the imaging quality parameters are effectively improved through our approach, which further demonstrates its superiority.

2) Case II: The imaging results obtained without correction for HF errors, and with correction through [36] and the proposed approach are, respectively, shown in Fig. 28(a)–(c), while Fig. 29 shows the scene Region 1 with sufficiently strong scattering targets of Fig. 28 to present the focusing details. From Fig. 29(a), we see that ghosts are introduced around the real target due to the HF errors. Moreover, the proposed approach is capable of removing these ghosts, whereas [36] cannot, as illustrated in Fig. 29(b)–(c). Analogously, Fig. 30
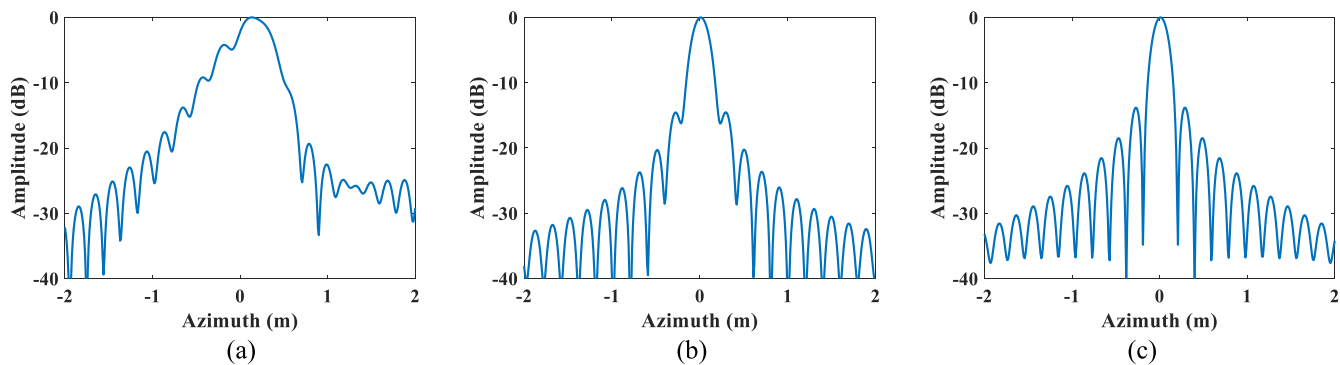
Fig. 20.   Azimuth profiles of target P01. (a) Without correction. (b) [26]. (c) Proposed approach.
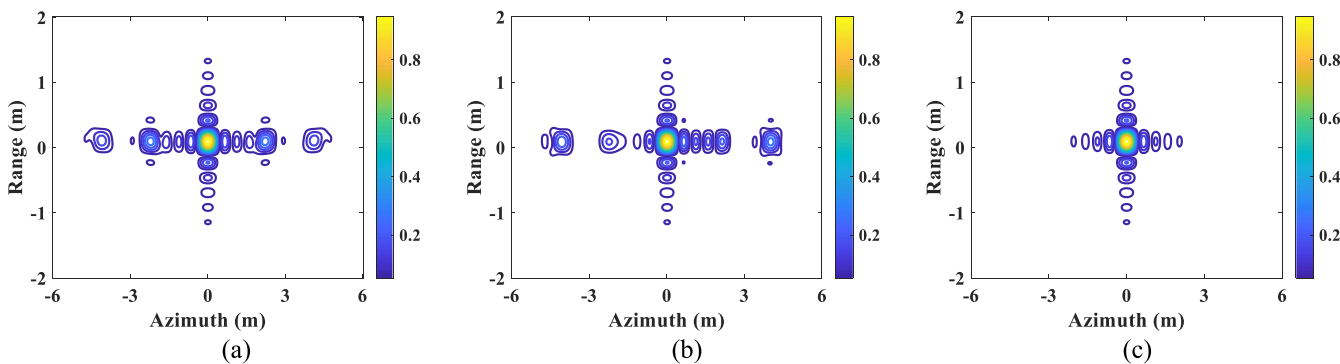

Fig. 21.   2-D IRFs of target P00. (a) Without correction. (b) [36]. (c) Proposed approach.
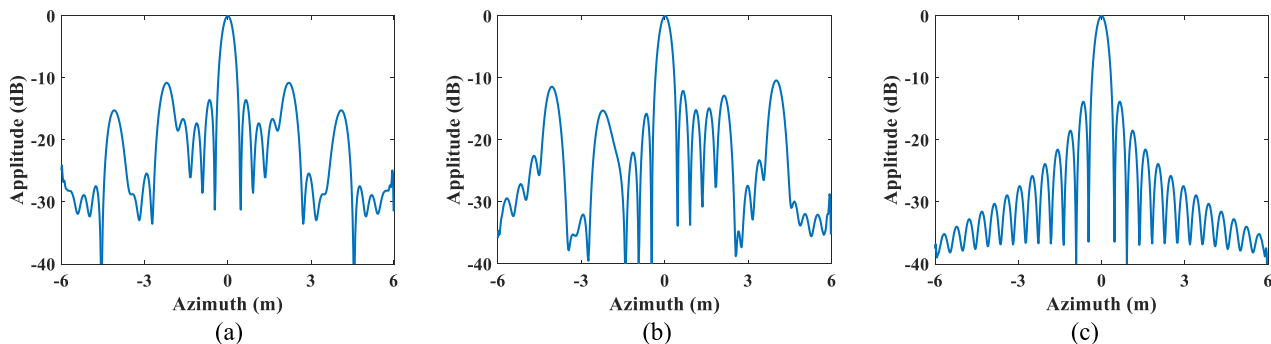

Fig. 22.   Azimuth profiles of target P00. (a) Without correction. (b) [36]. (c) Proposed approach.
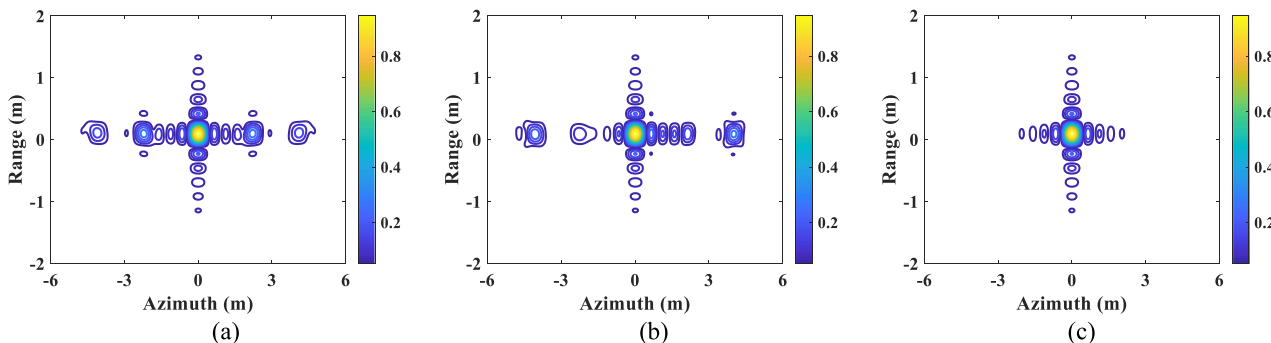

Fig. 23.   2-D IRFs of target P01. (a) Without correction. (b) [36]. (c) Proposed approach.
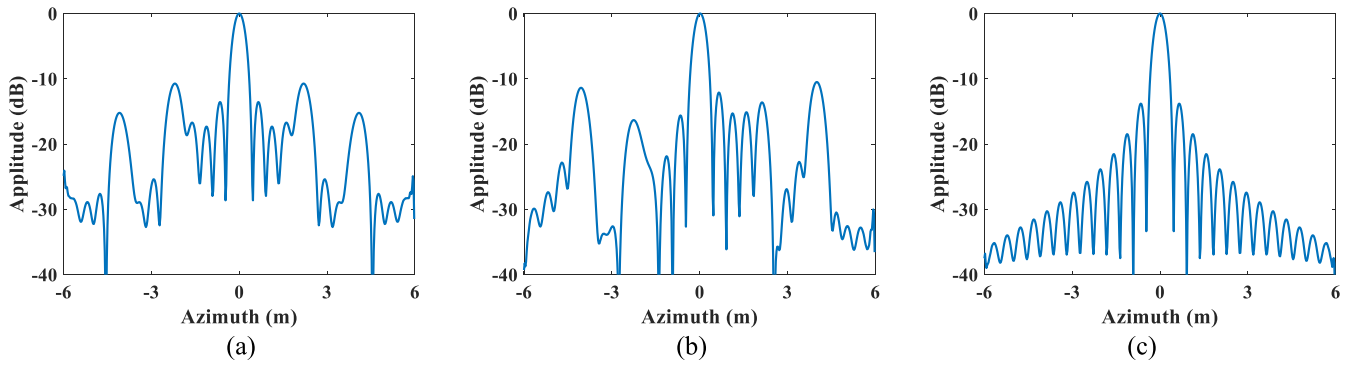
Fig. 24. Azimuth profiles of target P01. (a) Without correction. (b) [36]. (c) Proposed approach.
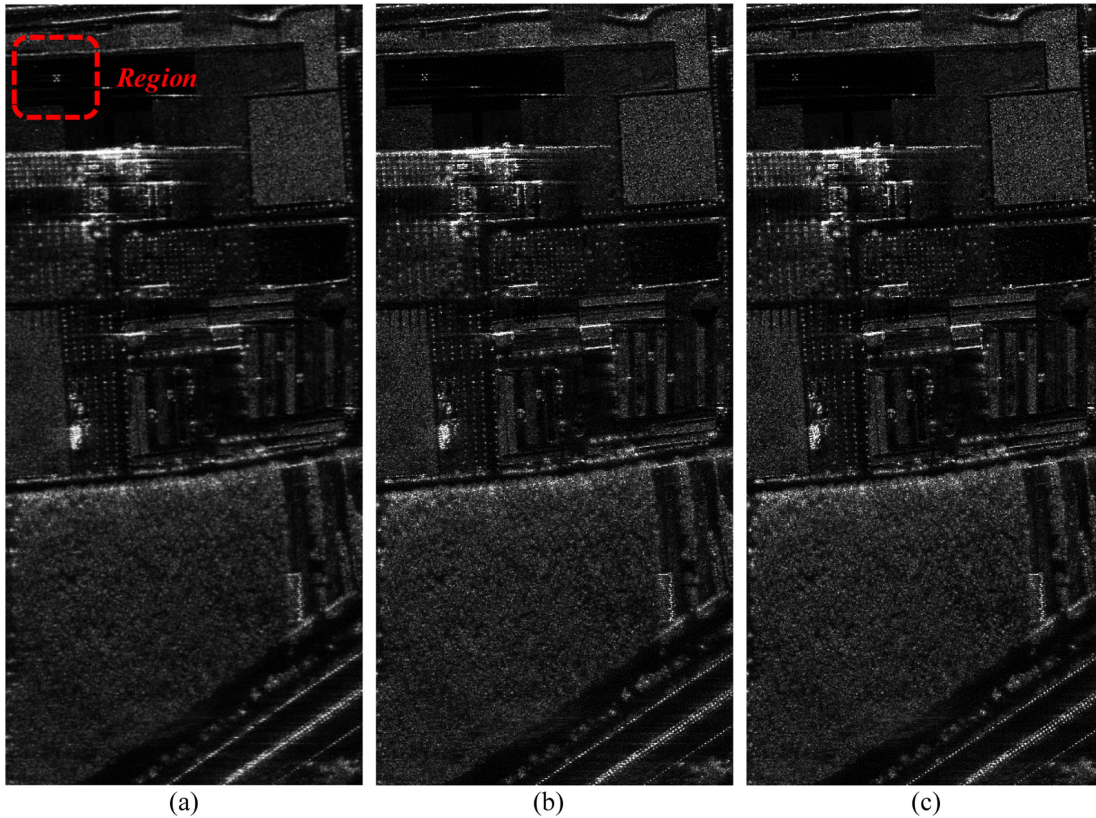

Fig. 25. Imaging results. (a) Without correction. (b) [26]. (c) Proposed approach.

plots the azimuth profiles of a selected scattering point acquired by different approaches, where the grating-lobes are marked, and the corresponding image quality parameters are tabulated in Table V. We can see that the grating-lobes of the target are eliminated and the image quality parameters are improved through our approach.

All real data are processed using MATLAB R2015b on a computer with an Intel Core i5-7300U CPU and 32.0 GB of RAM. The processing time of different methods are tabulated in Table VI. It can be seen that in Cases I and II, the proposed approach only increases the processing time by 8.3% and 5.6% compared to [26] and [36], respectively. Nonetheless, as a future

TABLE V
AZIMUTH IMAGE QUALITY PARAMETERS OF SELECTED TARGET IN CASE II

Method	IRW (m)	PSLR (dB)	ISLR (dB)
Without correction	0.29	−18.04	−14.52
[36]	0.24	−18.76	−14.91
Proposed	0.20	−25.54	−20.85

direction, we will optimize the implementation procedure of our approach to increase the processing efficiency, so as to better exert the advantages of multirotor UAV SAR.
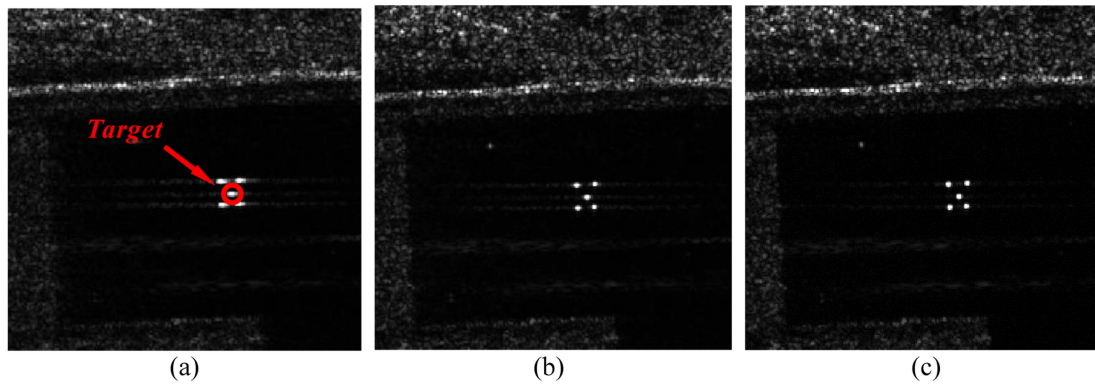
Fig. 26.   Selected scene of Fig. 25. (a) Without correction. (b) [26]. (c) Proposed approach.
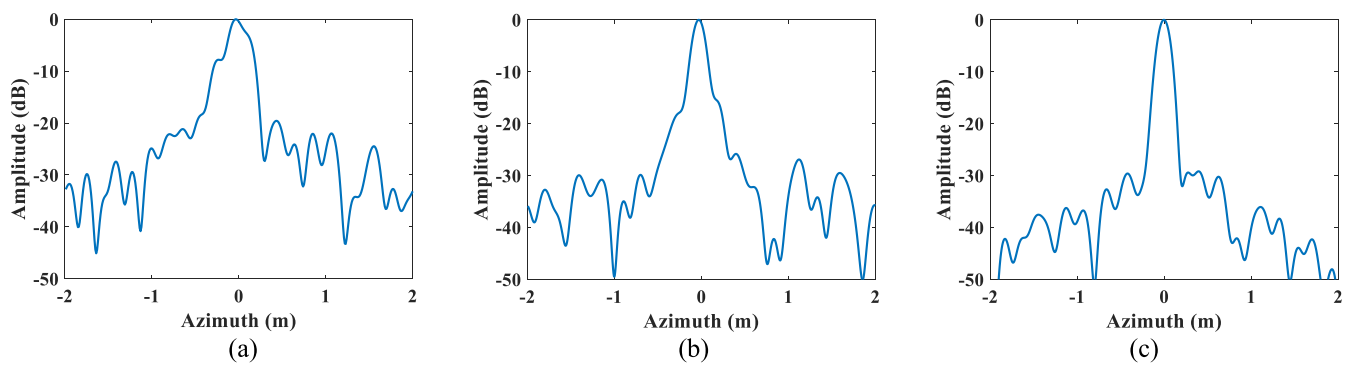

Fig. 27.   Azimuth profiles of the selected target. (a) Without correction. (b) [26]. (c) Proposed approach.
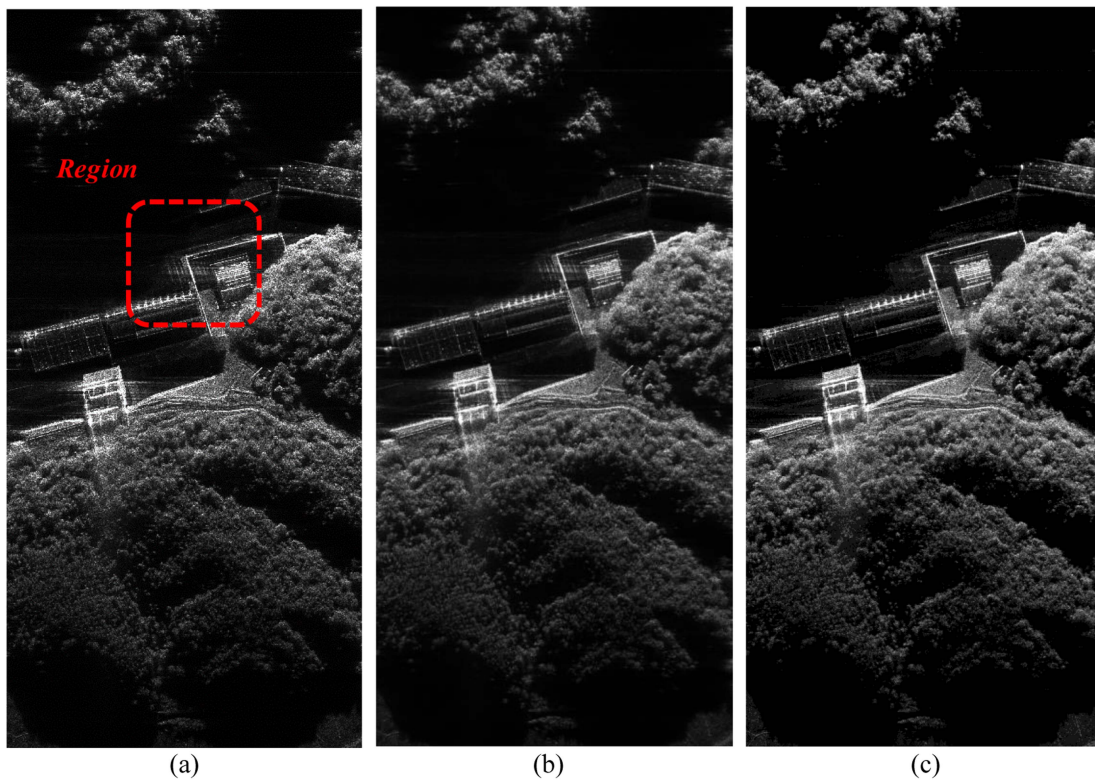

Fig. 28.   Imaging results. (a) Without correction. (b) [36]. (c) Proposed approach.
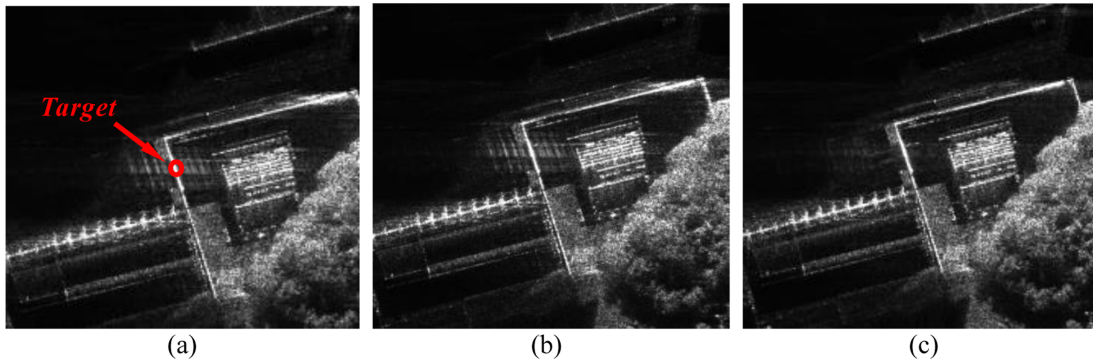
Fig. 29. Selected scene of Fig. 28. (a) Without correction. (b) [36]. (c) Proposed approach.
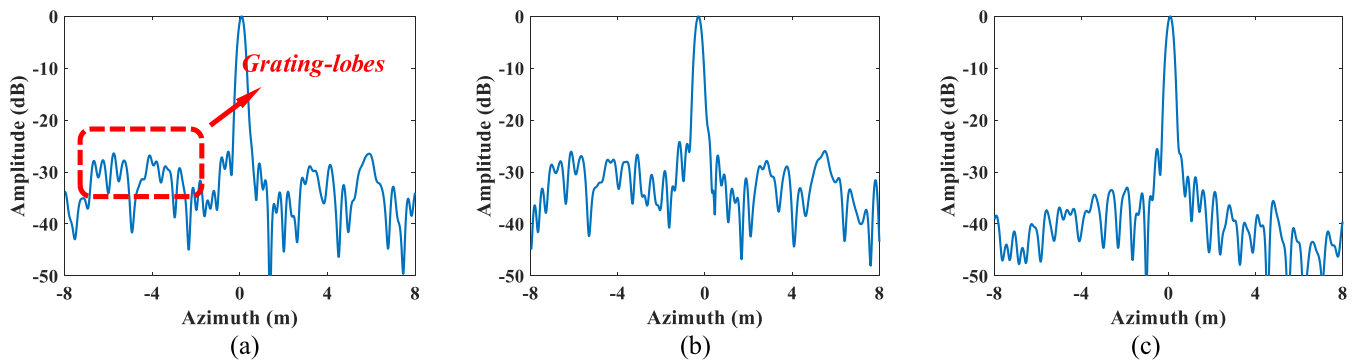

Fig. 30. Azimuth profiles of selected target. (a) Without correction. (b) [36]. (c) Proposed approach.

TABLE VI
PROCESSING TIME OF REAL DATA EXPERIMENT

	Method	Processing time
	Without correction	40 s
CASE I	[26]	48 s
	Proposed	52 s
	Without correction	30 s
CASE II	[36]	36 s
	Proposed	38 s

VI. CONCLUSION

As a new application platform for SAR, multirotor UAVs are widely used in various fields due to their low cost, high flexibility, and strong survival ability. However, the complex motion form and flight characteristics present challenges such as spatially variant LF errors and severe HF errors. To solve these issues, an improved MoCo approach is proposed for high-resolution multirotor UAV SAR imaging. First, a geometry model of multirotor UAV is established to effectively separate the complex range history into different parts and their influence on imaging quality is analyzed. Then, LF errors are eliminated by an improved two-step MoCo approach and HF errors are estimated and corrected by an extended PGA scheme. Finally, both simulation and experimental results demonstrate the effectiveness of the proposed approach for multirotor UAV SAR. As a future direction, we plan to optimize the entire processing flow and increase the processing efficiency, so as to better exert the advantages of multirotor UAV SAR.

APPENDIX A

To achieve scaling correction of the echo signal through CZT, the parameters of CZT are set as

$$A(\eta) = \exp\left\{-j\pi\left[1 + \alpha(\eta)\right]\right\} \qquad (A1)$$

$$W(\eta) = \exp\left\{-j\frac{2\pi}{N}\left[1 + \alpha(\eta)\right]\right\} \qquad (A2)$$

where $A(\eta)$ and $W(\eta)$ determine the frequency spacing and start frequency of the resampled range spectrum, respectively [39]. The compensation functions H_1 and H_2 in (19) and (20) can be rewritten as

$$H_1(n, \eta) = A^{-n}(\eta) \qquad (A3)$$

$$H_2(n, \eta) = W^{n^2/2}(\eta) \qquad (A4)$$

where n is an integer ranges from 0 to $N - 1$, i.e., $n = \tau/\Delta T$.

Then, resampling of echo signal at each azimuth time is implemented through several complex multiplications and Fourier transform as

$$S_0(f'_\tau, \eta) = \left[S_0(n, \eta) \cdot A^{-n}(n, \eta) \cdot W^{n^2/2}(n, \eta)\right]$$

$$\otimes W^{-n^2/2}(n, \eta) \cdot W^{n^2/2}(n, \eta)$$
$$= \sum S_0(n, \eta) \cdot A^{-n}(n, \eta) \cdot W^{nk}(n, \eta) \quad \text{(A5)}$$

where $S_0(n, \eta)$ is the discrete version of $S_0(\tau, \eta)$ and $\otimes$ denotes the convolution operator, which can be implemented through fast Fourier transform and multiplication. Substituting (A1) and (A2) into (A5), the scaling corrected echo signal becomes

$$S_0\{f'_\tau, \eta\} = S_0\{f_\tau \cdot [1 + \alpha(\eta)], \eta\}. \quad \text{(A6)}$$

REFERENCES

[1] W. G. Carrara, R. S. Goodman, and R. M. Majewski, *Spotlight Synthetic Aperture Radar: Signal Processing Algorithm*. Boston, MA, USA: Artech House, 1995.

[2] J. C. Curlander and R. N. McDonough, *Synthetic Aperture Radar: Systems and Signal Processing*. Hoboken, NJ, USA: Wiley, 1991.

[3] Y. Ren et al., "An improved spatially variant MOCO approach based on an MDA for high-resolution UAV SAR imaging with large measurement errors," *Remote Sens.*, vol. 14, no. 11, Jun. 2022, Art. no. 2670.

[4] I. G. Cumming and F. H. Wong, *Digital Processing of Synthetic Aperture Radar Data: Algorithm and Implementation*. Boston, MA, USA: Artech House, 2005.

[5] S. Kim et al., "Multichannel W-band SAR system on a multirotor UAV platform with real-time data transmission capabilities," *IEEE Access*, vol. 8, pp. 144413–144431, 2020.

[6] H. Shakhatreh et al., "Unmanned aerial vehicles (UAVs): A survey on civil applications and key research challenges," *IEEE Access*, vol. 7, pp. 48572–48634, 2019.

[7] T. Mizushima, R. Nakamura, and H. Hadama, "Reflection characteristics of ultra-wideband radar echoes from various drones in flight," in *Proc. IEEE Topical Conf. Wireless Sensors Netw.*, San Antonio, TX, USA, 2020, pp. 30–33.

[8] C. Zhang and J. M. Kovacs, "The application of small unmanned aerial systems for precision agriculture: A review," *Precis. Agriculture*, vol. 13, no. 6, pp. 693–712, Dec. 2012.

[9] T.-Z. Xiang, G.-S. Xia, and L. Zhang, "Mini-unmanned aerial vehicle-based remote sensing: Techniques, applications, and prospects," *IEEE Geosci. Remote Sens. Mag.*, vol. 7, no. 3, pp. 29–63, Sep. 2019.

[10] Y. Luomei, F. Xu, F. Wang, and Y. Dong, "Demonstration of simultaneous localization and imaging with multirotor-borne MiniSAR," *IEEE J. Sel. Topics Appl. Earth Observ. Remote Sens.*, vol. 15, pp. 6548–6558, 2022.

[11] W. Xu, B. Wang, M. Xiang, S. Wang, and Y. Jianfeng, "A novel motion compensation approach based on symmetric triangle wave interferometry for UAV SAR imagery," *IEEE Access*, vol. 8, pp. 104996–105007, 2020.

[12] L. Zhang, Z. Qiao, M.-D. Xing, L. Yang, and Z. Bao, "A robust motion compensation approach for UAV SAR imagery," *IEEE Trans. Geosci. Remote Sens.*, vol. 50, no. 8, pp. 3202–3218, Aug. 2012.

[13] J. Chen, B. Liang, D.-G. Yang, D.-J. Zhao, M. Xing, and G.-C. Sun, "Two-step accuracy improvement of motion compensation for airborne SAR with ultrahigh-resolution and wide swath," *IEEE Trans. Geosci. Remote Sens.*, vol. 57, no. 9, pp. 7148–7160, Sep. 2019.

[14] G. Fornaro and G. Franceschetti, "Motion compensation errors: Effects on the accuracy of airborne SAR images," *IEEE Trans. Aerosp. Electron. Syst.*, vol. 41, no. 4, pp. 1338–1352, Oct. 2005.

[15] S. Tang, L. Zhang, P. Guo, G. Liu, and G.-C. Sun, "Acceleration model analyses and imaging algorithm for highly squinted airborne spotlight-mode SAR with maneuvers," *IEEE J. Sel. Topics Appl. Earth Observ. Remote Sens.*, vol. 8, no. 3, pp. 1120–1131, Mar. 2015.

[16] Y. Wang, Z. Wang, B. Zhao, and L. Xu, "Compensation for high-frequency vibration of platform in SAR imaging based on adaptive chirplet decomposition," *IEEE Geosc. Remote Sens. Lett.*, vol. 13, no. 6, pp. 792–795, Jun. 2016.

[17] N. Marechal, "High frequency phase errors in SAR imagery and implications for autofocus," in *Proc. Int. Geosci. Remote Sens. Symp.*, Lincoln, NE, USA, 1996, pp. 1233–1240.

[18] B. Peng, X. Wei, B. Deng, H. Chen, Z. Liu, and X. Li, "A sinusoidal frequency modulation Fourier transform for radar-based vehicle vibration estimation," *IEEE Trans. Instrum. Meas.*, vol. 63, no. 9, pp. 2188–2199, Sep. 2014.

[19] Z. Wang, F. Liu, T. Zeng, and S. He, "A high-frequency motion error compensation algorithm based on multiple errors separation in BiSAR onboard mini-UAVs," *IEEE Trans. Geosci. Remote Sens.*, vol. 60, 2022, Art. no. 5223013.

[20] Y. Li, Q. Wu, J. Wu, P. Li, Q. Zheng, and L. Ding, "Estimation of high-frequency vibration parameters for terahertz SAR imaging based on FrFT with combination of QML and RANSAC," *IEEE Access*, vol. 9, pp. 5485–5496, 2021.

[21] O. O. Bezvesilniy, I. M. Gorovyi, and D. M. Vavriv, "Estimation of phase errors in SAR data by local-quadratic map-drift autofocus," in *Proc. Int. Radar Symp.*, Warsaw, Poland, May 2012, pp. 376–381.

[22] X. Wu and Z. Zhu, "A novel autofocus algorithm based on minimum entropy criteria for SAR images," *Syst. Eng. Electron.*, vol. 25, no. 7, pp. 867–869, Jul. 2003.

[23] J. Chen, B. Liang, J. Zhang, D.-G. Yang, Y. Deng, and M. Xing, "Efficiency and robustness improvement of airborne SAR motion compensation with High-Resolution and wide swath," *IEEE Geosci. Remote Sens. Lett.*, vol. 19, 2022, Art. no. 4004005.

[24] L. Zhang, M. Hu, G. Wang, and H. Wang, "Range-dependent map-drift algorithm for focusing UAV SAR imagery," *IEEE Geosci. Remote Sens. Lett.*, vol. 13, no. 8, pp. 1158–1162, Aug. 2016.

[25] S. Y. Aye, W. Liu, H. Feng, and B. P. Ng, "Study of multi-rotor UAV SAR processing," in *Proc. IEEE Radar Conf.*, Seattle, WA, USA, 2017, pp. 0226–0232.

[26] J. Chen, M. Xing, G.-C. Sun, and Z. Li, "A 2-D space-variant motion estimation and compensation method for ultrahigh-resolution airborne stepped-frequency SAR with long integration time," *IEEE Trans. Geosci. Remote Sens.*, vol. 55, no. 11, pp. 6390–6401, Nov. 2017.

[27] G. Fornaro, "Trajectory deviations in airborne SAR: Analysis and compensation," *IEEE Trans. Aerosp. Electron. Syst.*, vol. 35, no. 3, pp. 997–1009, Jul. 1999.

[28] Y. Zhang, J. Sun, P. Lei, and H. Wang, "High-frequency vibration compensation of helicopter-borne THz-SAR," *IEEE Trans. Aerosp. Electron. Syst.*, vol. 52, no. 3, pp. 1460–1466, Jun. 2016.

[29] Y. Gao, Z. Zhang, M. Xing, Y. Zhang, and Z. Li, "Paired echo suppression algorithm in helicopter-borne SAR imaging," *IET Radar Sonar Navigat.*, vol. 11, no. 11, pp. 1605–1612, Nov. 2017.

[30] W. Qu, W. Yang, and R. Zhang, "Frequency estimation method of sinusoidal frequency signal based on piecewise FFT," in *Proc. 11th Int. Conf. Wireless Commun., Netw. Mobile Comput.*, Shanghai, China, 2015, pp. 1–4.

[31] M. Xing, X. Jiang, R. Wu, F. Zhou, and Z. Bao, "Motion compensation for UAV SAR based on raw radar data," *IEEE Trans. Geosci. Remote Sens.*, vol. 47, no. 8, pp. 2870–2883, Aug. 2009.

[32] L. Yang, M. Xing, Y. Wang, L. Zhang, and Z. Bao, "Compensation for the NsRCM and phase error after polar format resampling for airborne spotlight SAR raw data of high-resolution," *IEEE Geosci. Remote Sens. Lett.*, vol. 10, no. 1, pp. 165–169, Jan. 2013.

[33] Y. L. Neo, F. Wong, and I. G. Cumming, "A two-dimensional spectrum for bistatic SAR processing using series reversion," *IEEE Geosci. Remote Sens. Lett.*, vol. 4, no. 1, pp. 93–96, Jan. 2007.

[34] S. Chen, Y. Wang, and R. Cao, "A high frequency vibration compensation approach for ultra-high resolution SAR imaging based on sinusoidal frequency modulation fourier-bessel transform," *J. Syst. Eng. Electron.*, vol. 34, no. 4, pp. 894–905, Aug. 2023.

[35] R. Bamler, "A comparison of range-Doppler and wavenumber domain SAR focusing algorithms," *IEEE Trans. Geosci. Remote Sens.*, vol. 30, no. 4, pp. 706–713, Jul. 1992.

[36] D. E. Wahl, P. H. Eichel, D. C. Ghiglia, and C. V. Jakowatz, "Phase gradient autofocus-A robust tool for high-resolution SAR phase correction," *IEEE Trans. Aerosp. Electron. Syst.*, vol. 30, no. 3, pp. 827–835, Jul. 1994.

[37] D. Zhu, R. Jiang, X. Mao, and Z. Zhu, "Multi-subaperture PGA for SAR autofocusing," *IEEE Trans. Aerosp. Electron. Syst.*, vol. 49, no. 1, pp. 468–488, Jan. 2013.

[38] Y. Ren, S. Tang, P. Guo, L. Zhang, and H. C. So, "2-D spatially variant motion error compensation for high-resolution airborne SAR based on range-Doppler expansion approach," *IEEE Trans. Geosci. Remote Sens.*, vol. 60, 2022, Art. no. 5201413.

[39] D. Zhu and Z. Zhu, "Range resampling in the polar format algorithm for spotlight SAR image formation using the chirp z-transform," *IEEE Trans. Signal Process.*, vol. 55, no. 3, pp. 1011–1023, Mar. 2007.

Jiahao Han was born in Shaanxi Province, China. He received the B.S. degree in electrical information engineering in 2020 from Xidian University, Xi'an, China, where he is currently working toward the Ph.D. degree in information and communication engineering with the National Key Lab of Radar Signal Processing.

His major research interests include unmanned aerial vehicle SAR imaging and motion compensation.

Ping Guo was born in Shandong Province, China. She received the B.S. degree in electrical engineering from the Qufu Normal University, Qufu, China, and the Ph.D. degree in signal processing with the National Laboratory of Radar Signal Processing, Xidian University, Xi'an, China, in 2011 and 2016, respectively.

She is currently a Lecturer with the College of Communication and Information Engineering, Xi'an University of Science and Technology, Xi'an. Her research interests mainly include imaging of several SAR modes, moving target detection, and imaging.

Shiyang Tang (Member, IEEE) was born in Jiangsu Province, China. He received the B.S. and Ph.D. degrees in electrical engineering from Xidian University, Xi'an, China, in 2011 and 2016, respectively.

He is currently a Professor with the National Key Laboratory of Radar Signal Processing, Xidian University. His research interests include imaging of SAR with curved path, and high-speed moving target detection and imaging.

Yinan Li (Member, IEEE) was born in Shaanxi Province, China. He received the M.S. degree in electrical engineering from Xidian University, Xi'an, China, in 2010.

He is currently a Professor with the China Academy of Space Technology, Xi'an. He has participated in the development of the microwave radiometers for the FY-3 satellite and HY-2 satellite successively. He is currently, the Chief Designer, and developing the synthetic aperture radiometer for the ocean salinity satellite of China. His research interests include system design and calibration.

Zhanye Chen was born in Hubei Province, China. He received the B.S., M.S., and Ph.D. degrees in electrical engineering from Xidian University, Xi'an, China, in 2013, 2015, and 2019, respectively.

He is currently an Associate Professor with the State Key Laboratory of Millimeter Waves, Southeast University, Nanjing, China. His research interests include moving target indication, radar imaging, and radar simulation.

Linrang Zhang was born in Shaanxi Province, China. He received the M.S. and Ph.D. degrees in electrical engineering from Xidian University, Xi'an, China, in 1991 and 1999, respectively.

He is currently a Full Professor with the National Key Laboratory of Radar Signal Processing, Xidian University. He has authored or coauthored three books and published over 100 papers. His research interests include radar system analysis and simulation, radar signal processing, and jamming suppression.

Yi Ren was born in Shaanxi Province, China. He received the B.S. and Ph.D. degrees in electrical engineering from the National Key Laboratory of Radar Signal Processing, Xidian University, Xi'an, China, in 2018 and 2022, respectively.

His major research interests include SAR imaging and motion compensation.

Hing Cheung So (Fellow, IEEE) was born in Hong Kong. He received the B.Eng. degree from the City University of Hong Kong, Kowloon, Hong Kong, in 1990 and the Ph.D. degree from The Chinese University of Hong Kong, Hong Kong, in 1995, both in electronic engineering.

From 1990 to 1991, he was an Electronic Engineer with the Research and Development Division, Everex Systems Engineering Ltd., Hong Kong. During 1995–1996, he was a Postdoctoral Fellow with The Chinese University of Hong Kong. From 1996 to 1999, he was a Research Assistant Professor with the Department of Electronic Engineering, City University of Hong Kong, where he is currently a Professor. His research interests include detection and estimation, fast and adaptive algorithms, multidimensional harmonic retrieval, robust signal processing, source localization, and sparse approximation.

Dr. So has been on the editorial boards of *IEEE Signal Processing Magazine* (2014–2017), IEEE TRANSACTIONS ON SIGNAL PROCESSING (2010–2014), *Signal Processing* (2010–), and *Digital Signal Processing* (2011–). He was also the Lead Guest Editor for *IEEE Journal of Selected Topics in Signal Processing*, special issue on "Advances in Time/Frequency Modulated Array Signal Processing" in 2017. In addition, he was an elected member in Signal Processing Theory and Methods Technical Committee (2011–2016) of the IEEE Signal Processing Society, where he was the Chair of the awards subcommittee (2015–2016).

Zhixin Lian was born in Shaanxi Province, China. She received the B.S. degree in electrical information engineering in 2021 from Xidian University, Xi'an, China, where she is currently working toward the Ph.D. degree in information and communication engineering with the National Key Lab of Radar Signal Processing.

Her research interests include heterogeneous image registration and scene matching positioning.